Electronic Supplementary Information for Chemical Science

Tracking the Picosecond Deactivation Dynamics of a Photoexcited Iron Carbene Complex by Time-Resolved X-ray Scattering

Denis Leshchev[a]*, Tobias C. B. Harlang[b,c], Lisa A. Fredin[d], Dmitry Khakhulin[e], Yizhu Liu[f], Elisa Biasin[c], Mads G. Laursen[c], Gemma E. Newby[a], Kristoffer Haldrup[c], Martin M. Nielsen[c], Kenneth Wärnmark[f], Villy Sundström[b], Petter Persson[d], Kasper S. Kjær[b,c], Michael Wulff[a]*

[a]*European Synchrotron Radiation Facility, 71 Avenue des Martyrs, 38000 Grenoble, France*
[b]*Department of Chemical Physics, Lund University, P.O. Box 12 4, 22100 Lund, Sweden*
[c]*Molecular Movies Group, Department of Physics, Technical University of Denmark, DK-2800, Lyngby, Denmark*
[d]Theoretical Chemistry Division, Lund University, P.O. Box 124, 22100 Lund, Sweden
[e]*European XFEL GmbH, Holzkoppel 4, 22869 Schenefeld, Germany*
[f]*Centre for Analysis and Synthesis, Department of Chemistry, Lund University, Lund P.O. Box 12 4, 22100 Sweden*

S1 Experimental procedure

Time-resolved wide angle x-ray scattering (TRWAXS) data have been acquired on the beamline ID09B at European Synchrotron Radiation Facility (ESRF) using the pump-probe technique[1]. In brief, optical pulses from a Ti:Sapphire laser (986 Hz rep-rate), synchronized to single X-ray pulses, were passed through a TOPAS system (parametric amplifier) to get 1.2 ps pulses with the wavelength λ = 485 nm, which corresponds to the MLCT absorption band of the studied complex[2]. The laser beam was focused to get the spot size of 260 μm (FWHM) on the sample. With additional attenuation the pulse energy of the laser was adjusted to 40 μJ / pulse. The structural changes have been probed with 100-ps x-ray pulses from the storage ring passed through the ID09b chopper system that reduces the X-ray repetition rate down to 986 Hz. The x-rays were focused to a 90×60 hμm×vμm spot on the sample. As mentioned in the main text, the TRWAXS data was collected in two separate runs by using two different x-ray energies, 18 keV and 25.2 keV. By using multilayer optics the energy bandwidth of the incident x-rays was set to 1.9% and 1.6% for 18 keV and 25.2 keV data collection runs respectively. The scattered x-rays were detected with an area detector, FReLoN[3], placed at 43 mm from the sample. For 18 keV measurements, the exposure time per x-ray scattering image was 5 seconds with the count rate of ~4000 cts/sec in the liquid peak. A data set consisting of 17 time points was collected by measuring 2000 “laser-on” and 500 “laser-off” images. For 25.2 keV measurements, the exposure time per x-ray image was 10 seconds with count rate of ~1000 cts/sec in the liquid peak. Single time point difference pattern was obtained by measuring 900 ‘laser-on” and 900 “laser-off” images.

The choice of the time delay for collection of the 25.2 keV data was based on the knowledge about the system acquired from the previous spectroscopic measurements[2] and known temporal resolution of the setup (100 ps). According to the optical results, the vibrational cooling of the complex in ^{5}MC state takes 31 ps. Taking into account the duration of the synchrotron pulses,100 ps, the scattering data collected at 150 ps gives access to the structure of the fully relaxed excited state, explaining the choice of the time delay. It has to be noted that fitting of the 18 keV data set using the relaxed ^{5}MC molecular geometry have provided satisfactory results indicating insensitivity of present measurements to the vibrational cooling step in deactivation of the MLCT state of $[Fe(btbip)_2]^{2+}$.

A 9 mM acetonitrile solution of $[Fe(btbip)_2]^{2+}$ was used as a sample during the experiment The complex was prepared according to procedure described previously.[2] The solution was flushed through a 300 um thick sapphire nozzle with a speed of ~3 m/s in order to ensure that each pump-probe event will appear on a new portion of sample. No sample degradation was observed during the experiment. The total optical density of the sample was 3.5. While this value can be considered as high for optical spectroscopy experiments, the x-ray experiments performed here require high concentrations of the sample for maximizing the pump-probe signal.

S2 Density functional theory calculations

The ground state (GS), ^{3}MC, and ^{5}MC geometries of the complex were freely optimized using PBE0,[4–6] which is known to give good agreement to experimental structures[7–9], and triple-ζ 6-311G(d,p)[10–12] with a complete acetonitrile polarizable continuum model (PCM)[13] in Gaussian G09[14]. Optimized minima were each relaxed with no symmetry constraints, allowing for all possible Jahn-Teller effects, and from multiple starting geometries, including the GS structure and a geometry where all bond lengths were expanded at least 0.3 Å. The fully optimized excited state local minima were identified and can be clearly distinguished, from the significant change in spin density on Fe, as MC like. The geometry of the PBE0 optimized minima are summarized in the main text and more completely in ESI-Table 1. These geometries were used for the calculation of the associated TRWAXS signals.

The PBE0 optimized ^{3}MC structure has one axis expanded, which leads to one ligand being further away from the Fe than the other. While symmetry restricted calculations often align the d_{z2} orbital along the axial bonds of tridentate ligands, symmetry unrestricted optimizations allow any linear combination of orbitals and so that asymmetric distortions in the equatorial plane are possible. Previous calculations on related Fe-NHC complexes show that four bond expanded in a plane and one axis distorted ^{3}MCs have similar energies,[15] however both structures preferentially expand the equatorial ligand bonds, which might be related to the lower reorganization of this expansion compared to the ligand axial expansion. Running a PBE0 triplet optimization starting with ^{5}MC geometry of $[Fe(btbip)_2]^{2+}$, which has all Fe-ligand bonds expanded and thus should be closer to the more typical d_{x2-y2} expansion, results in the one-distorted-axis ^{3}MC described in Table 1 and ESI-Table 1.

In order to investigate the effect of functional choice on the MC state energy, we have calculated energies of ^{3}MC and ^{5}MC states using various functionals at the PBE0 geometries. The results are summarized in ESI-Table 2. PBE0-D3[16] adds dispersion functionals which might be important in capturing ligand-ligand interactions like those in Jahn-Teller distortions, however it offers similar energies to traditional PBE0.[17] Any future fully computational studies could explore the effect of dispersion on the optimized minima. B3LYP[18] is one of the most ubiquitous hybrid functionals and CAMB3LYP[19] includes coulomb interactions, both give similar energies to PBE0. TPSS[20–22] is a pure functional and over estimates the excited state energies significantly. B3LYP*[23,24] has exact exchange in between B3LYP and PBE0.

Since the ^{5}MC energy obtained with B3LYP* is in best agreement with the experiment, we have also fully optimized the GS, ^{3}MC, and ^{5}MC minima with B3LYP*. As a result, we find that the GS and ^{5}MC geometries derived from PBE0 and B3LYP* are very similar in respect to Fe-ligand

bond distances and angles. On the other hand, two separate ^{3}MC structures could be distinctly optimized with B3LYP*. One of the ^{3}MC structures obtained with B3LYP* has a single axis expanded and is very similar to the PBE0 optimized ^{3}MC. The other one shows the four equatorial bonds expanded. These two states are practically isoenergetic, right in line with the multidimensional potential energy surfaces of the methyl-analog, $[Fe(bmip)_2]^{2+}$ (bmip = 2,6-bis(3-methyl-imidazol-1-ylidene)pyridine), where the d_{z2} and d_{x2-y2} like ^{3}MCs geometries were identified.[15] We compare all the relaxed triplet and quintet MCs from PBE0 and B3LYP* to the TRWAXS signal in SI-Figure 3.

ESI-Table 1. Structural parameters of the Fe first coordination shell in the $[Fe(btbip)_2]^{2+}$ complex for the ground state (GS), ^{3}MC, and ^{5}MC states optimized using PBE0/6-311G(d,p)/PCM(MeCN).

	GS (^{1}MC)	^{3}MC	^{5}MC
Mulliken spin density on Fe	-	2.06	3.81
R_{ax} (Å) ($Fe\text{-}N_{Py}$)	1.94 ± 0.00	2.10 ± 0.10	2.23 ± 0.0001
R_{eq} (Å) ($Fe\text{-}C_{NHC}$)	2.10 ± 0.0004 (I)[b]	2.11 ± 0.00 (I)[b]	2.32 ± 0.002 (I)[b]
	2.10 ± 0.00 (II)[b]	2.27 ± 0.0001 (II)[b]	2.32 ± 0.0005 (II)[b]
R_{total} (Å)	2.04 ± 0.03	2.16 ± 0.04	2.29 ± 0.02
O (°)[c]	8.02	10.78	13.83
P (°)	0.09	0.006	0.58
Avg. Bite angle (°)	106.60 ± 0.01	107.42 ± 3.58	110.96 ± 0.03

[a]Calculated from crystallographic data.[2]

[b]Marks I and II correspond to the ligand numbering.

[c]O is the octahedricity-value and P is the planarity both of which measure the average deviation of the set of ligand-Fe-ligand and ligand dihedral angles, respectively, from their “ideal” values, where “ideal” first coordination angles are 90° and dihedral angles are 0°. Calculated as average deviation =(∑|ideal angle-measured angle|)/n.

ESI-Table 2. Functional dependence of energies (in eV) at the PBE0 optimized minima. All calculations were done using the 6-311G(d,p) basis set and a PCM(MeCN) model. The experimental value is also shown for comparison.

	PBE0	PBE0-D3	B3LYP	B3LYP*	CAMB3LYP	TPSS	Experiment
GS	0.00	0.00	0.00	0.00	0.00	0.00	0.00
^{3}MC	0.74	0.69	0.76	0.95	0.98	1.46	-
^{5}MC	0.13	0.16	0.32	0.72	0.16	1.71	0.75 ± 0.15

ESI-Table 3. Energies and structural parameters of the Fe first coordination shell in the $[Fe(btbip)_2]^{2+}$ complex for the ground state (GS), ^{3}MC, and ^{5}MC states optimized using B3LYP*/6-311G(d,p)/PCM(MeCN) and for ^{5}MC state obtained from experiment.

	GS (^{1}MC)		^{3}MC		^{5}MC	
	Calc.	Exp.[a]	Calc. (dx^2-y^2)	Calc. (dz^2)	Calc.	Exp.
E (eV)	0	0	0.92	0.95	0.73	0.75 ± 0.15
Fe spin density	-	-	1.98	2.03	3.74	-
R_{ax} (Å)[c] ($Fe-N_{Py}$)	1.94	1.939	1.94 (I)[b]	2.04 (I)[b]	2.22	2.23 ± 0.03
			2.00 (II)[b]	2.17 (II)[b]		
R_{eq} (Å)[c] ($Fe-C_{NHC}$)	2.12	2.096	2.23 (I)	2.13 (I)	2.33	2.31 ±0.02
			2.32 (II)	2.29 (II)		
O (°)[d]	8.00	8.04	9.12	10.62	13.34	-
P (°)[d]	0.04	2.33	0.01	0.004	0.42	-
Avg. Bite Angle (°)	106.83	106.41 ± 0.14	112.71	107.70	111.20	-

[a]Calculated from crystallographic data.[2]

[b]Marks I and II correspond to the ligand numbering.

[c]The standard deviations of the calculated bond lengths and angles were found to be at most 0.001 Å.

[d]O is the octahedricity-value and P is the planarity both of which measure the average deviation of the set of ligand-Fe-ligand and ligand dihedral angles, respectively, from their “ideal” values, where “ideal” first coordination angles are 90° and dihedral angles are 0°. Calculated as average deviation =(∑|ideal angle-measured angle|)/n.

S3 Molecular dynamics simulations

The ground and excited state DFT structures of $[Fe(btbip)_2]^{2+}$ were solvated in a cubic box (50 Å size) of acetonitrile molecules using the three-site interaction potential derived by Guardia et. al.[25]. The bond lengths of the solute molecule were constrained and MD trajectories were calculated with OPLS2005 force field parameters[26] and a Nose-Hoover thermostat at 300 K[27]. The system was equilibrated for 1 ns and, afterwards, the trajectories were recorded for total time of 2 ns. The radial distribution functions (RDFs) of the solute-solvent atom pairs were sampled on 0.01 A radial bins with more than 2000 time steps. From the RDFs, the cage contribution to the difference scattering signal was calculated according to the procedure described previously[28].

S4 Molecular structure in the ^{5}MC state as a function of structural parameters R_{ax} and R_{eq}

The functional dependence between selected parameters (R_{ax}, R_{eq}) and the overall molecular structure was obtained in the following way. First, we introduced a grid of parameter values consisting of 9 points. As initial point we took R_{ax} and R_{eq} bond lengths obtained in DFT optimization of the ^{5}MC geometry and then varied these values by 0.03 Å. Then at each point of the grid we performed a DFT optimization of the structure using PBE0/6-311G(d,p)/PCM(MeCN) as described above in DFT methods. Here however, we freezed the bond lengths R_{ax} and R_{eq} while allowing the rest of the ligands to relax. Finally, having Cartesian XYZ coordinates of each of the 99 atoms as a function of two parameters we used interpolation to obtain XYZ coordinates at values of the parameters located in between the 9 grid points. The illustration of each step is shown in SI-Figure 1 (a-c). After the structure is parameterized, the calculation of the associated TRWAXS signals is done according to the Debye formula. Finally, using this signal as a function of (R_{ax}, R_{eq}) structural refinement can be performed. Examples of calculated TRWAXS signals for nine grid points are shown in SI-Figure 1d.

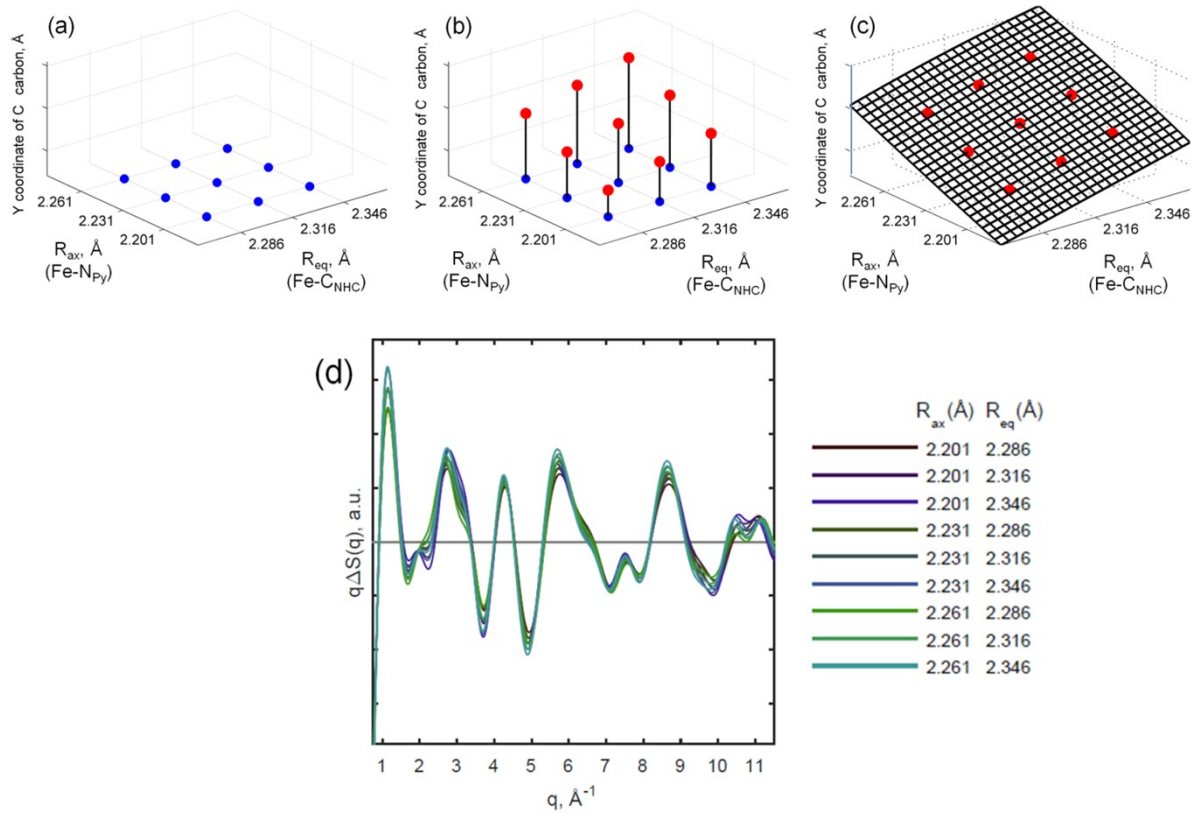

ESI-Figure-1. a) The concept of the introduced parameter grid (R_{ax}, R_{eq}) consisting of 9 points including the initial value from the DFT optimization. b) After performing the constrained DFT calculations at each point of the grid, one obtains 9 values of each of the XYZ coordinates of each atom. For illustration purposes, Y coordinate of one of the carbon atoms in the first coordination shell of Fe was selected. c) Interpolation between the points for each of the XYZ coordinates of each atom allows obtaining the functional dependence between molecular structure and the selected parameters. d) Calculated TRWAXS signals for nine points of the grid.

S5 Data analysis

The collected scattering data was reduced according to the standard protocols[29–31]. An established TRWAXS analysis framework was used for interpretation of the experimental signal. The signal is considered to be due to changes in the solute structure and its solvation shell reorganization (cage term) and changes in the bulk solvent due to changes in the temperature and density:

$$\Delta S(q,t) = \frac{1}{R}\gamma(t)[\Delta S_{solute}(q) + \Delta S_{cage}(q)] + \Delta T(t)\frac{\partial(S(q))}{\partial T}|_{\rho} + \Delta\rho(t)\frac{\partial(S(q))}{\partial \rho}|_{T} \quad (1)$$

where R is the ratio between numbers of solvent and solute molecules; $\gamma(t)$, $\Delta T(t)$ and $\Delta\rho(t)$ are time dependent changes in excited state fraction, temperature and density respectively. The solute and cage related terms were calculated based on the density functional theory (note S3) and molecular dynamics (note S3) calculations, respectively. The solute contribution was calculated according to standard procedure using Debye equation[30] whereas the cage scattering was calculated using procedure described below in S4. The solvent related contributions $\frac{\partial(S(q))}{\partial T}|_{\rho}$ and $\frac{\partial(S(q))}{\partial \rho}|_{T}$ were measured separately according to the standard procedure using azobenzene dye molecules.[32] The fitting of the TRWAXS data by the model in equation (1) structural parameters, excited state fraction and temperature rise in Kelvin. The latter two parameters are utilized for the thermodynamic analysis described in the main text and below.

Data fitting was performed by using the classical χ^2 estimator defined as

$$\chi^2 = \sum_q \left(\frac{\Delta S_{th}(q,t) - \Delta S_{exp}(q,t)}{\sigma(q,t)}\right)^2 \quad (2)$$

where $\Delta S_{th}(q,t)$, $\Delta S_{exp}(q,t)$ and $\sigma(q,t)$ correspond to theoretical curve, experimental data and experimental error, respectively. For model comparison we have used the reduced estimator defined as $\chi^2_{red} = \chi^2/(N-p-1)$, where N is the number of points and p is the number of parameters.

As described in the main text, the density term in equation 2 was excluded from the analysis (note S6). The fitting of the data with ^{5}MC signal, temperature differential and density term was compared to the same fitting but without density term (SI Figure 2). Both fits result in essentially the same χ^2_{red} values showing that addition of density term does not significantly improve the fit quality and hence should be removed from the model. The same result was found for all investigated time delays in 18 keV data set, as well as for 25.2 keV data. This is in contrast with the previous works on other prototype complexes such as $[Fe(bpy)_3]^{2+}$ and $[Fe(terpy)_2]^{2+}$[33,34]. The TRWAXS measurements on aqueous solutions of these complexes have found the increase in the density of the sample upon promotion to the quintet ^{5}MC state. As an explanation of this effect, the earlier theoretical work was employed[35]. There it was shown that due to overall expansion of the molecule upon transition between ground and ^{5}MC state, one of the water molecules is repulsed from the ligand enclosure. This molecule is then injected into

the bulk solvent causing the change in the density. The fact that we do not observe such an effect in present work can be related to the solvent molecule size effect. Since MeCN molecules have larger size comparing to water, it is more difficult for them to intercalate into ligand structure of $[Fe(btbip)_2]^{2+}$ and therefore similar injection process does not appear and density change is not observed.

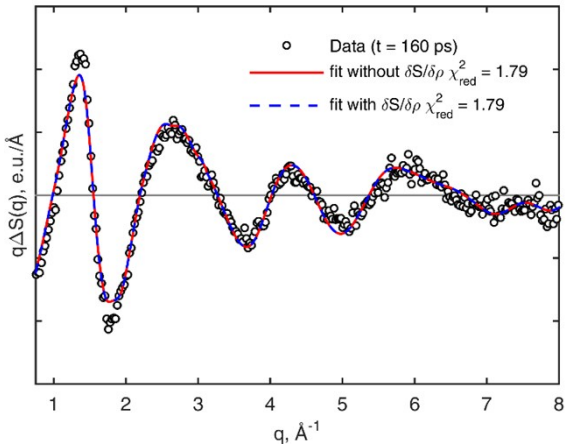

ESI-Figure 2. Fitting of the 18 keV data at 160 ps by the model with and without density term.

In order to determine whether the excited state is ^{3}MC and ^{5}MC, two corresponding signals were fitted to the 25.2 keV curve using equation (1) and determination of best-fit values of $\Delta T(t)$ and $\gamma(t)$ at t = 150 ps. The fitting results indicated that ^{5}MC state described data the best. As mentioned in the main text, the fit and the data disagree in the low-q part (q<2.5 Å^{-1}) which is likely due to oversimplification of the cage term. Hence, in order to get insight into solute structure alone we fitted ^{3}MC and ^{5}MC signals to the high-q (q>2.5 Å^{-1}) portion of the data (ESI-Figure 3). Corresponding χ^2_{red} values for the fits are summarized in ESI-Table 3. The contrast between the χ^2_{red} values for ^{3}MC and ^{5}MC is more significant, therefore further supporting the ^{5}MC assignment. We note that while fitting the low-q part requires inclusion the cage term, focusing only on high-q portion of the data allows to omit its contribution as it does not affect corresponding χ^2_{red} values (ESI-Table 3).

Further analysis have shown that B3LYP* functional provides the value of the energy difference between GS and ^{5}MC state that is consistent with the thermodynamic analysis (see below). Here we demonstrate that the ^{5}MC molecular geometries obtained using B3LYP* and PBE0 functionals are similar and consistent with the experiment. SI Figure 3 shows the fitting results of the models to 25.2 keV data. Since the corresponding χ^2_{red} values appear to be close to each other we conclude that both structures are consistent with the experiment within signal-to-noise. The ^{3}MC geometries obtained from B3LYP* calculations are also shown for completeness. The analysis includes only high-q part of the data so that the signal associated with the cage term can be omitted.

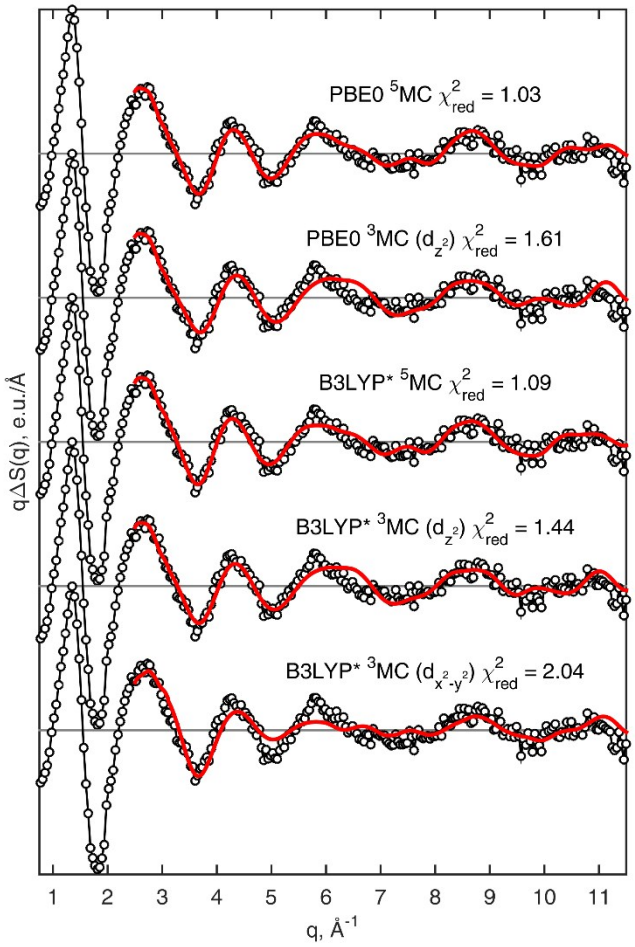

SI-Figure 3. Comparison of fits of 25.2 keV data with ^{3}MC and ^{5}MC signals calculated using PBE0 and B3LYP* functionals.

SI-Table 3. χ^2_{red} values for fitting the 25.2 keV data with molecular geometries for 3MC and 5MC states obtained with PBE0 and B3LYP* functionals.

Functional	State	χ^2_{red}			
		$0.75 \le q \le 11.5$ Å^{-1}		$2.5 \le q \le 11.5$ Å^{-1}	
		with cage contr.	without cage contr.	with cage contr.	without cage contr.
PBE0	^{5}MC	1.60	4.41	1.03	1.03
	^{3}MC (d_{z^2})	1.88	4.14	1.56	1.61
B3LYP*	^{5}MC	-	4.75	-	1.09
	^{3}MC (d_{z^2})	-	4.25	-	1.44
	^{3}MC($d_{x^2-y^2}$)	-	5.52	-	2.04

Further refinement of the molecular geometry in ^{5}MC state was performed using the structural model described in the text using equation (1) and minimization of the estimator (2). Since the fitting of the data in this case was performed using only high-q portion of the data (q≥2.5 Å^{-1}) the cage term in equation (1) was omitted due to its insignificance in this region. The fitting

procedure was used to refine R_{ax} and R_{eq}, parameters used for parameterization of molecular structure of $[Fe(btbip)_2]^{2+}$ in ^{5}MC state (note S5), as well as $\gamma(t)$ and $\Delta T(t)$ at t = 150 ps.

The 18 keV data was fitted using global fitting procedure which ties population dynamics of the excited state to the hydrodynamics of the solvent. Detailed description of this procedure is available in the literature[29,30,36]. The following provides main equations used for data fitting. First, the fraction of the molecules in the ^{5}MC state is described by exponential decay:

$$\gamma(t) = \gamma_0 exp(-t/\tau), \quad (3)$$

where γ_0 and τ are the initial excited state fraction and the ^{5}MC lifetime respectively. Second, the temperature of the solvent (in K) as a function of time can be calculated as follows:

$$T(t) = \frac{V_{mol} N_A}{C_V} c_{tot} \gamma_0 [h\nu - \Delta E\, exp(-t/\tau)] + T_{offset}, \quad (4)$$

where V_{mol} is molar volume of MeCN (in m^3/mol); N_A is Avogadro number; C_V is specific heat capacity of MeCN at constant volume (in J/(mol*K)); c_{tot} is total concentration of $[Fe(btbip)_2]^{2+}$ molecules in the sample (in mM); $h\nu$ is the photon energy (in J); ΔE is the energy difference between ^{5}MC and GS states (in J); T_{offset} is the offset temperature discussed in the text. Note that this expression is correct only for short time delays where the sample expansion due to pressure gradients is negligible. The characteristic time of this process is determined by a/v_s, where a is the laser spot size (1σ) and v_s is the speed of sound in MeCN[36,37]. In case of present measurements the characteristic time scale is ~200 ns, which is much longer than the maximum time delay investigated (1 ns), which therefore validates the choice of the framework. In order to perform the data fitting the expressions (3) and (4) were numerically convoluted with the instrument response function with FWHM of A_{x-ray} and corrected for the time zero t_0 uncertainty. The obtained expressions were used in equation (1). The fitting was performed by refinement of parameters A_{x-ray}, t_0, γ_0, τ, ΔE and T_{offset} by minimizing estimator (2) with additional summation over time delays.

Finally, to estimate the additional excited state fraction γ_{offset} which could potentially contribute to T_{offset} the following expression was used:

$$\gamma_{offset} = T_{offset}\left[\frac{V_{mol} N_A}{C_V} c_{tot} h\nu\right]^{-1} \quad (5)$$

All the fits were performed using home-written routines in MATLAB. For structural fits of 25.2 keV data the uncertainties of the fitting parameters were estimated using procedure similar to the one applied for treatment of extended x-ray absorption fine structure data (EXAFS).[38–40] Briefly, the uncertainties are estimated using the inversion of Hessian matrix calculated after fitting the data in q-space and then scaled by a factor determined by the Nyquist limit on the data information content. The latter is derived as follows. First, the data, its uncertainties and theoretical curve are transformed from reciprocal q-space to real r-space via Fourier transform. The spacing between the points in r-space is determined by Nyquist theorem which insures the points to be statistically independent from each other[41]. Second, a new χ^2_{red} value is calculated using Fourier transformed data, uncertainties and theory defined on r-grid up to r_{max} determined by the size of the molecule which is about 12 Å for $[Fe(btbip)_2]^{2+}$. Finally, the scaling factor for

uncertainties is calculated as $\sqrt{\chi^2_{red}}$. The overall procedure for estimating uncertainties was described in detail previously[42]. For global fitting of 18 keV data, the scaling factor obtained from individual time points was found to be almost constant, so the average scaling factor was used to scale the uncertainty values obtained from the Hessian inversion.

S6. Estimation of the excited state fraction and temperature change from optical density of the sample

The expected excited state fraction and corresponding temperature rise due to the de-excitation of the molecules can be estimated as follows.[32] By using the laser spot size ($d = 260\ \mu m$, FWHM) and the pulse energy ($E = 40\ \mu J/pulse$), the fluency on the sample can be estimated as $E_0 = \frac{4Eln(2)}{\pi d^2} = 0.052\ J/cm^2$. By using the path length inside of the liquid jet ($L = 300\ \mu m$), the latter can be transformed into the value of peak energy per volume: $E_V = \frac{E}{L} = 1.74\ J/cm^3$. Assuming identical centers for the laser and x-ray beams and by knowing x-ray size parameters (horizontal and vertical FWHMs are $h_x = 60\ \mu m$ and $w_x = 90\ \mu m$,respectively), the average laser energy per volume in the volume probed by x-rays can be calculated as $E_{sample} = \frac{d}{\sqrt{(d+h_x)(d+w_x)}} E_V = 1.35\ J/cm^3$. Given that the optical density of the sample in this experiment was ~ 3.5, and that the reflectivity of the jet at normal incidence is $R = \left|\frac{1-n}{1+n}\right|^2$ (where n is the refractive index which for MeCN is 1.346, hence giving $R = 0.022$), the average energy deposited by the laser pulse into the volume probed by x-rays is $\Delta E = E_{sample}(1 - 10^{-3.5})(1 - 0.022) = 1.32\ J/cm^3$. Finally, given that the isochoric heat capacity of MeCN is $C_V = 1.24 \frac{J}{K\ cm^3}$, the expected temperature rise at $1\ ns$ time delay is $\Delta T = \frac{\Delta E}{C_V} = 1.06\ K$, which, by using equation (5), can be translated to the expected total excited state fraction of 58 %. Both of these values are in fair agreement with the observed values, supporting the conclusions regarding the thermodynamic values derived from the experiment.

References

1 M. Wulff, A. Plech, L. Eybert, R. Randler, F. Schotte and P. Anfinrud, *Faraday Discuss.*, 2003, **122**, 13–26.

2 Y. Liu, T. Harlang, S. E. Canton, P. Chábera, K. Suárez-Alcántara, A. Fleckhaus, D. a Vithanage, E. Göransson, A. Corani, R. Lomoth, V. Sundström and K. Wärnmark, *Chem. Commun.*, 2013, **49**, 6412–6414.

3 J.-C. Labiche, O. Mathon, S. Pascarelli, M. A. Newton, G. G. Ferre, C. Curfs, G. Vaughan, A. Homs and D. F. Carreiras, *Rev. Sci. Instrum.*, 2007, **78**, 91301.

4 M. Ernzerhof and G. E. Scuseria, *J. Chem. Phys.*, 1999, **110**, 5029.

5 C. Adamo and V. Barone, *J. Chem. Phys.*, 1999, **110**, 6158.

6 E. Brémond and C. Adamo, *J. Chem. Phys.*, 2011, **135**, 24106.

7 L. a. Fredin, M. Pápai, E. Rozsályi, G. Vankó, K. Wärnmark, V. Sundström and P. Persson, *J. Phys. Chem. Lett.*, 2014, **5**, 2066–2071.

8 G. A. Parada, L. A. Fredin, M.-P. Santoni, M. Jäger, R. Lomoth, L. Hammarström, O. Johansson, P. Persson and S. Ott, *Inorg. Chem.*, 2013, **52**, 5128–37.

9 Y. Liu, K. S. Kjaer, L. a. Fredin, P. Chábera, T. Harlang, S. E. Canton, S. Lidin, J. Zhang, R. Lomoth, K.-E. Bergquist, P. Persson, K. Wärnmark and V. Sundström, *Chemistry*, 2014, **21**, 3628–3639.

10 A. D. McLean and G. S. Chandler, *J. Chem. Phys.*, 1980, **72**, 5639–5648.

11 R. Krishnan, J. S. Binkley, R. Seeger and J. A. Pople, *J. Chem. Phys.*, 1980, **72**, 650–

654.
12 K. Raghavachari and G. W. Trucks, *J. Chem. Phys.*, 1989, **91**, 1062–1065.
13 G. Scalmani and M. J. Frisch, *J. Chem. Phys.*, 2010, **132**, 114110.
14 M. J. Frisch, G. W. Trucks, H. B. Schlegel, G. E. Scuseria, M. A. Robb, J. R. Cheeseman, G. Scalmani, V. Barone, B. Mennucci, G. A. Petersson, H. Nakatsuji, M. Caricato, X. Li, H. P. Hratchian, A. F. Izmaylov, J. Bloino, G. Zheng, J. L. Sonnenberg, M. Hada, M. Ehara, K. Toyota, R. Fukuda, J. Hasegawa, M. Ishida, T. Nakajima, Y. Honda, O. Kitao, H. Nakai, T. Vreven, J. A. Montgomery Jr., J. E. Peralta, F. Ogliaro, M. Bearpark, J. J. Heyd, E. Brothers, K. N. Kudin, V. N. Staroverov, R. Kobayashi, J. Normand, K. Raghavachari, A. Rendell, J. C. Burant, S. S. Iyengar, J. Tomasi, M. Cossi, N. Rega, J. M. Millam, M. Klene, J. E. Knox, J. B. Cross, V. Bakken, C. Adamo, J. Jaramillo, R. Gomperts, R. E. Stratmann, O. Yazyev, A. J. Austin, R. Cammi, C. Pomelli, J. W. Ochterski, R. L. Martin, K. Morokuma, V. G. Zakrzewski, G. A. Voth, P. Salvador, J. J. Dannenberg, S. Dapprich, A. D. Daniels, O. Farkas, J. B. Foresman, J. V Ortiz, J. Cioslowski and D. J. Fox, *Gaussian, Inc., Wallingford CT, 2016, Gaussian 09, Revis. D.01*.
15 L. a. Fredin, M. Pápai, E. Rozsályi, G. Vankó, K. Wärnmark, V. Sundström and P. Persson, *J. Phys. Chem. Lett.*, 2014, **5**, 2066–2071.
16 S. Grimme, J. Antony, S. Ehrlich and H. Krieg, *J. Chem. Phys.*, 2010, **132**, 154104.
17 D. N. Bowman and E. Jakubikova, *Inorg. Chem.*, 2012, **51**, 6011–6019.
18 A. D. Becke, *J. Chem. Phys.*, 1993, **98**, 5648–5652.
19 T. Yanai, D. P. Tew and N. C. Handy, *Chem. Phys. Lett.*, 2004, **393**, 51–57.
20 J. Tao, J. P. Perdew, V. N. Staroverov and G. E. Scuseria, *Phys. Rev. Lett.*, 2003, **91**, 146401.
21 V. N. Staroverov, G. E. Scuseria, J. Tao and J. P. Perdew, *J. Chem. Phys.*, 2003, **119**, 12129–12137.
22 V. N. Staroverov, G. E. Scuseria, J. Tao and J. P. Perdew, *J. Chem. Phys.*, 2004, **121**, 11507.
23 M. Reiher, O. Salomon and B. Artur Hess, *Theor. Chem. Acc.*, 2001, **107**, 48–55.
24 O. Salomon, M. Reiher and B. A. Hess, *J. Chem. Phys.*, 2002, **117**, 4729–4737.
25 E. Guàrdia, R. Pinzón, J. Casulleras, M. Orozco and F. J. Luque, *Mol. Simul.*, 2001, **26**, 287–306.
26 W. L. Jorgensen, D. S. Maxwell and J. Tirado-Rives, *J. Am. Chem. Soc.*, 1996, **118**, 11225–11236.
27 G. J. Martyna, M. L. Klein and M. Tuckerman, *J. Chem. Phys.*, 1992, **97**, 2635–2643.
28 A. O. Dohn, E. Biasin, K. Haldrup, M. M. Nielsen, N. E. Henriksen and K. B. Møller, *J. Phys. B At. Mol. Opt. Phys.*, 2015, **48**, 244010.
29 H. Ihee, M. Lorenc, T. K. Kim, Q. Y. Kong, M. Cammarata, J. H. Lee, S. Bratos and M. Wulff, *Science*, 2005, **309**, 1223–1227.
30 H. Ihee, M. Wulff, J. Kim and S. Adachi, *Int. Rev. Phys. Chem.*, 2010, **29**, 453–520.
31 K. Haldrup, M. Christensen and M. Meedom Nielsen, *Acta Crystallogr. Sect. A Found. Crystallogr.*, 2010, **66**, 261–269.
32 K. S. Kjær, T. B. van Driel, J. Kehres, K. Haldrup, D. Khakhulin, K. Bechgaard, M. Cammarata, M. Wulff, T. J. Sørensen, M. M. Nielsen, K. S. Kjaer, T. B. van Driel, J. Kehres, K. Haldrup, D. Khakhulin, K. Bechgaard, M. Cammarata, M. Wulff, T. J. Sorensen and M. M. Nielsen, *Phys. Chem. Chem. Phys.*, 2013, **15**, 15003–16.
33 K. Haldrup, G. Vankó, W. Gawelda, A. Galler, G. Doumy, A. M. March, E. P. Kanter, A. Bordage, A. Dohn, T. B. Van Driel, K. S. Kjær, H. T. Lemke, S. E. Canton, J. Uhlig, V. Sundström, L. Young, S. H. Southworth, M. M. Nielsen and C. Bressler, *J. Phys. Chem. A*, 2012, **116**, 9878–9887.
34 G. Vankó, A. Bordage, M. Pápai, K. Haldrup, P. Glatzel, A. M. March, G. Doumy, A. Britz, A. Galler, T. A. Assefa, D. Cabaret, A. Juhin, T. B. van Driel, K. S. Kjær, A. O. Dohn, K. B. Moller, H. T. Lemke, E. Gallo, M. Rovezzi, Z. Németh, E. Rozsályi, T. Rozgonyi, J. Uhlig, V. Sundstrom, M. M. Nielsen, L. Young, S. H. Southworth, C. Bressler and W. Gawelda, *J. Phys. Chem. C*, 2015, **119**, 5888–5902.
35 L. M. L. Daku and A. Hauser, *J. Phys. Chem. Lett.*, 2010, **1**, 1830–1835.
36 F. Mirloup, Universite Paris VI, 2004.

37 M. Cammarata, M. Lorenc, T. K. Kim, J. H. Lee, Q. Y. Kong, E. Pontecorvo, M. Lo Russo, G. Schiró, a. Cupane, M. Wulff and H. Ihee, *J. Chem. Phys.*, 2006, **124**, 124504.
38 E. Curis and S. Bénazeth, *J. Synchrotron Radiat.*, 2000, **7**, 262–266.
39 C. H. Booth and Y.-J. Hu, *J. Phys. Conf. Ser.*, 2009, **190**, 12028.
40 B. Ravel and M. Newville, *J. Synchrotron Radiat.*, 2005, **12**, 537–541.
41 E. A. Stern, *Phys. Rev. B*, 1993, **48**, 9825–9827.
42 D. Leshchev, *PhD Thesis, Univ. Grenoble Alpes*, 2016, Reaction dynamics of small molecules in solution.